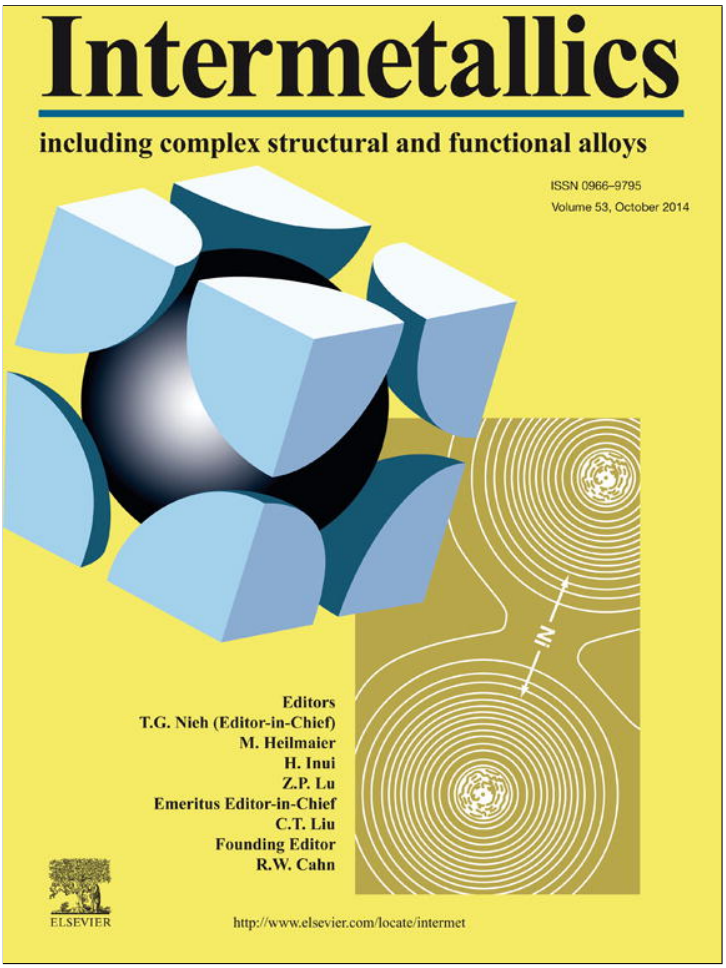

Intermetallics 53 (2014) 120–128

Contents lists available at ScienceDirect

Intermetallics

journal homepage: www.elsevier.com/locate/intermet

Accelerated precipitation in the AFA stainless steel Fe–20Cr–30Ni–2Nb–5Al via cold working

Geneva Trotter [a], Garrett Rayner [a], Ian Baker [a,*], Paul R. Munroe [b]

[a] Thayer School of Engineering, Dartmouth College, Hanover, NH 03755-8000, USA
[b] Materials Science and Engineering, University of New South Wales, Sydney, NSW 2052, Australia

ARTICLE INFO

Article history:
Received 17 February 2014
Received in revised form
25 April 2014
Accepted 28 April 2014
Available online 21 May 2014

Keywords:
A. Laves phases
B. Phase identification
B. Precipitates
C. Heat treatment
C. Plastic forming, cold
D. Microstructure

ABSTRACT

The effects of cold work on the microstructural evolution during aging of a solutionized alumina-forming austenitic stainless steel, Fe–20Cr–30Ni–2Nb–5Al (at.%), were investigated using scanning electron microscopy, transmission electron microscopy, and scanning transmission electron microscopy. Cold work prior to aging at either 700 °C or 800 °C facilitated the heterogeneous precipitation of both Laves phase and B2-type NiAl precipitates. While often co-located after cold work, these particles were distinct. γ′-Ni_3Al precipitates were also observed in samples aged at 700 °C with 90% prior cold work. Compared to material that had not been strained, defects introduced by 50 and 90% cold work at 700 °C and 90% cold work at 800 °C not only caused a more rapid precipitation in the matrix but also an increase in the total volume fraction of precipitates as compared to material that had been simply aged.

1. Introduction

AFAs (alumina-forming austenitic stainless steels) are a new promising class of steels with potential for use in a number of energy-conversion applications [1–9]. For example, there is a current effort to develop power plant materials with excellent creep strength and corrosion resistance at temperatures >760 °C. Increasing the operating temperature improves efficiency with the added benefit of reducing CO_2 emissions [10–13]. The relatively low cost of ferritic steels make them desirable candidates, but they have yet to show the creep strength and oxidation resistance needed at high temperatures. Nickel-based superalloys can be used at temperatures in excess of 760 °C, but their high cost makes them less desirable for most applications [12,13]. In order for an AFA to be a viable alternative, it must have a strength and creep resistance that are close to or exceed those of Ni-based alloys. AFAs have relied on MC carbides for strength [1,3,4,14], but at temperatures greater than 800 °C there is concern that the carbides formed could coarsen and dissolve [4].

Further refinement of the Fe_2Nb Laves phase particles has potential to improve the creep life and high temperature strength of AFAs. Fe_2Nb Laves phase particles have shown long-term stability at high temperatures [14–17]. However, previous studies that looked to Laves phase particles for strength have only seen low or moderate creep resistance [14,17]. Decreasing the precipitate size and increasing the volume fraction would enable the precipitates to effectively pin dislocations and extend creep life. A Laves phase dispersion with particles less than 100 nm in diameter is recommended to obtain creep-levels on-par with MC carbide strengthened austenitic stainless steels [17].

One pathway to reducing the size and increasing the volume fraction of Laves phase precipitates in the matrix is to nucleate precipitates on dislocations. Nucleation on dislocations is an effect first modeled by Cahn [18] in 1957 and occurs because it lowers the total strain energy of an embryo. In order to effectively reduce the interfacial energy, precipitates that nucleate on dislocations should be well-matched on at least one matrix plane so they are able to form low-energy coherent or semi-coherent interfaces [19]. Images of Fe_2Nb that has precipitated in austenite alloys that have the base components of AFAs (Fe–20Cr–35Ni–2Nb and Fe–20Cr–25Ni–2Nb) [15] show strain contrast in TEM images that is indicative of a semi-coherent precipitate-matrix interface, making Fe_2Nb a promising candidate for precipitation on dislocations in AFA-type alloys.

Prestraining via cold work introduces dislocations that could dramatically affect the precipitation of the Laves phase, similar to

* Corresponding author. Tel.: +1 603 646 2184.
E-mail address: Ian.Baker@Dartmouth.edu (I. Baker).

http://dx.doi.org/10.1016/j.intermet.2014.04.018
0966-9795/

what has been observed in previous studies of other precipitate systems [20–23]. The effectiveness of prestraining before aging in changing microstructure and improving material properties depends on characteristics of the particular alloy system analyzed and the synergy of a number of different variables including, but not limited to: aging temperature, the amount of prestrain, and competing precipitation phenomena. For example, the improved hardness observed in a copper-bearing steel that had been prestrained prior to aging at 300 °C was attributed to additional particle nucleation on dislocations or excess vacancies arising from prestraining, however at an aging temperature of 500 °C the prestrain had little effect on hardness or particle nucleation [21]. In aluminum alloys cold work has been shown to have different effects depending on the alloy system, with dislocations enhancing hardening by providing nucleation sites for precipitates in the Al–Cu, Al–Cu–Mg, and Al–Cu–Li systems, while not proving effective for hardening in other aluminum systems [24]. Severe plastic deformation by cold rolling at room temperature followed by subsequent aging has been shown to improve both strength and ductility in a high strength Al–Mg–Si alloy [23] as well as a Cu–Ag alloy [22]. An increase in precipitation after cold work has been observed with other precipitates in alloys more closely related to AFAs. HTUPS (high-temperature ultrafine-precipitation-strengthened steel) alloys, modified for Al_2O_3 formation, are cold worked to enhance the precipitation of nanoscale MC carbide precipitates during creep [1,14,25]. While aging studies on AFA-type alloys have been done in the past [16], Laves phase precipitates have yet to be targeted via a combined aging and cold working approach.

In this study, the effect of cold work on a solution-annealed AFA-type alloy, Fe–20Cr–30Ni–2Nb–5Al (at.%) was investigated by comparing samples that had received cold work prior to aging to those that were simply aged. Microstructural analysis was performed using a scanning electron microscope (SEM), a transmission electron microscope (TEM) and a scanning transmission electron microscope (STEM) and energy dispersive spectroscopy (EDS). In addition, the effect of cold work and aging on the hardness of the material was examined.

2. Experimental

Fe–20Cr–30Ni–2Nb–5Al (at.%) ingots were arc melted and drop cast into a copper mold 15.2 cm long × 2.5 cm in diameter under argon. Common cast features [26] were observed: there was some segregation and a central pore was created during the solidification process. The as-cast material was homogenized in vacuum for 24 h at 1250 °C, then water-quenched. This solutionizing treatment was used since SEM investigations confirmed that it enabled the formation of a solutionized single phase matrix.

Specimens were milled to 4 mm × 4 mm × ~13 mm, and some were cold-rolled with approximately a 0.3 mm reduction per pass until the desired thickness reduction (50 or 90% ± 1%) was achieved. Unrolled, 50% rolled, and 90% rolled samples were aged in air for 24 h and 240 h at 700 °C, and for 2.4, 24, and 240 h at 800 °C. The resulting microstructures were examined using a FEI XL30 field emission gun (FEG) SEM operated at 15 kV and a FEI Tecnai F20ST FEG TEM operated at 200 kV, both equipped with EDS. For SEM examination samples were mechanically polished to a mirror finish using 0.05 μm alumina powder in a water suspension. TEM samples 3 mm in diameter and ~100 μm thick were electrolytically thinned using a twin-jet electropolisher at about −20 °C and 11V in a solution of 25% nitric acid in methanol. TEM specimens were examined using a Phillips CM200 FEG STEM operated at 200 kV that allowed for elemental mapping via EDS. Vickers hardness testing was conducted using a Leitz MINIload tester under a load of 1.96 N (200 g) with a 15 s dwell time at room temperature. No less than 10 indents were made for each condition.

SEM images taken at 8000× were processed and analyzed using ImageJ [27]. BSE images were used for particle analysis since BSE atomic number contrast allowed for optimal differentiation and detection of the matrix, Laves phase, and NiAl precipitates. The image processing routine included contrast enhancement followed by thresholding to include bright or dark contrasted regions to delineate Laves or NiAl particles, respectively. Images were then despeckled and outlier filters were run and small artifacts removed in the final binarized image. The particle parameters calculated include area fraction and equivalent circle diameter given as $2(A/\pi)^{1/2}$, of a circle with equivalent area A. SEM resolution limits and image quality was taken into account in order to minimize error. Segmented areas that had low pixel counts that corresponded to particles with a diameter smaller than 20–60 nm were excluded from the results.

3. Results

Fig. 1 shows bright-field TEM images with accompanying selected area diffraction (SAD) patterns of precipitates observed in Fe–20Cr–30Ni–2Nb–5Al (at.%). After the solution treatment the average grain size was 865 μm. Fig. 1(a) and (b) shows microstructural features after the alloy was aged at 800 °C for 24 h and Fig. 1(c) shows the alloy after 50% cold work prior to aging at 240 h. TEM examination confirmed that the alloy had an f.c.c. austenitic (γ) matrix (Fig. 1(a)) and that the lighter precipitates observed in the SEM backscattered electron (BSE) images (see

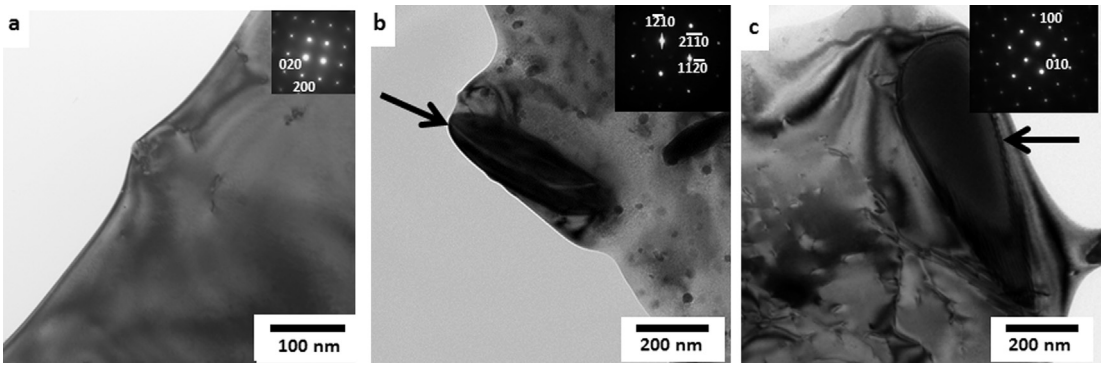

Fig. 1. Bright field TEM images of Fe–20Cr–30Ni–2Nb–5Al along [001] and corresponding selected area diffraction patterns of a) matrix after aging at 800 °C for 24 h; b) C14 hexagonal Fe_2Nb precipitate (arrowed) after aging at 800 °C for 24 h; and c) B2 NiAl precipitate (arrowed) after 50% cold work prior to aging at 240 h.

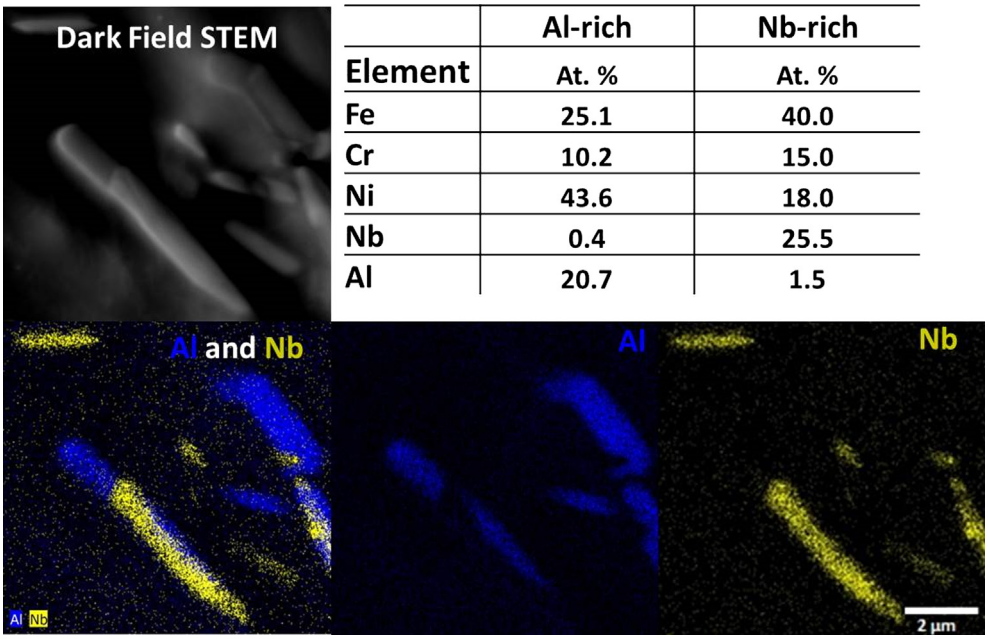

	Al-rich	Nb-rich
Element	At. %	At. %
Fe	25.1	40.0
Cr	10.2	15.0
Ni	43.6	18.0
Nb	0.4	25.5
Al	20.7	1.5

Fig. 2. Dark field STEM image and energy dispersive X-ray maps of Al and Nb in 50% cold-rolled Fe–20Cr–30Ni–2Nb–5Al aged 240 h at 800 °C. The table presents EDS spectra data on the composition of the aluminum and niobium-rich precipitates.

later) are C14-type Fe_2Nb phase (Fig. 1(b)) and that the darker precipitates are B2-ordered NiAl (Fig. 1(c)). The presence of both Laves phase and NiAl precipitates is in agreement with previous TEM analysis on precipitates in this alloy [17] and is typical of AFA-type alloys [1–9].

After sufficient aging and/or prior cold work Laves phase and B2–NiAl precipitates often appear interconnected. For example, Fig. 2 shows a dark field STEM image and EDS elemental maps of a specimen reduced by 50% and then aged for 240 h at 800 °C. The EDS maps and spectral data of Laves and B2-precipitates reveal that while the nickel makes up a large component of the matrix, it couples with the aluminum and is concentrated in the NiAl particles. Compared to the Al-rich B2 precipitate, the Nb-rich Laves phase precipitate has a lower aluminum (1.5 at.% vs. 20.7 at.%) and nickel (18 at.% vs. 43.6 at.%) content, and a higher iron (40 at.% vs. 25.1 at.%), chromium (15.0 at.% vs. 10.2 at.%) and aluminum (25.5 at.% vs. 0.4 at.%) content. The EDS maps also reveal that while often co-located after cold work, the NiAl and Fe_2Nb precipitates are distinct. TEM investigation of specimens after 90% cold work followed by aging at 700 °C show the presence of fine γ′-Ni_3Al ($L1_2$) precipitates (Fig. 3). These precipitates have been observed in creep rupture samples of this alloy at 750 °C 100 MPa and were noted to improve creep resistance [17].

Microstructural changes are shown as a function of rolling reduction and annealing time after aging at 700 °C in Fig. 4. When the Fe–20Cr–30Ni–2Nb–5Al (at.%) alloy is as-aged at 700 °C without prior cold work, no Laves phase precipitates were visible in the BSE images of the matrix up to 240 h (Fig. 4(a) and (d)). With cold work prior to aging at 700 °C both the B2 and Laves phase particles are globular in shape and are almost always coupled together in the matrix (Fig. 4(b), (c), (e) and (f)). Specimens with 50% (Fig. 4(b)) and 90% (Fig. 4(c)) cold work prior to aging for 24 h at 700 °C had a non-uniform, but fine distribution of Laves phase particles with slightly larger B2 particles in the matrix. A similar pattern of increased precipitation after cold work was observed after a 240 h anneal at 700 °C (Fig. 4(d)–(f)).

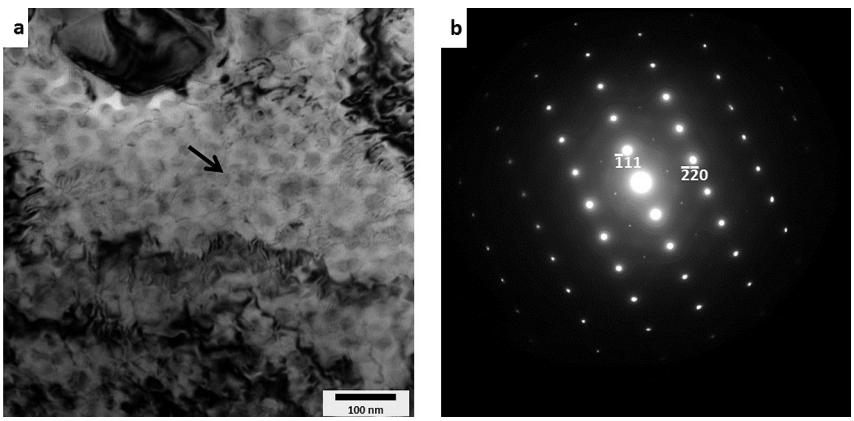

Fig. 3. a) Bright field TEM image of Fe–20Cr–30Ni–2Nb–5Al matrix (arrowed) after 90% rolling reduction followed by aging 240 h at 700 °C along $[1\bar{1}2]$; b) Corresponding selected area diffraction pattern taken from matrix showing γ′-Ni_3Al $L1_2$ supperlattice reflections.

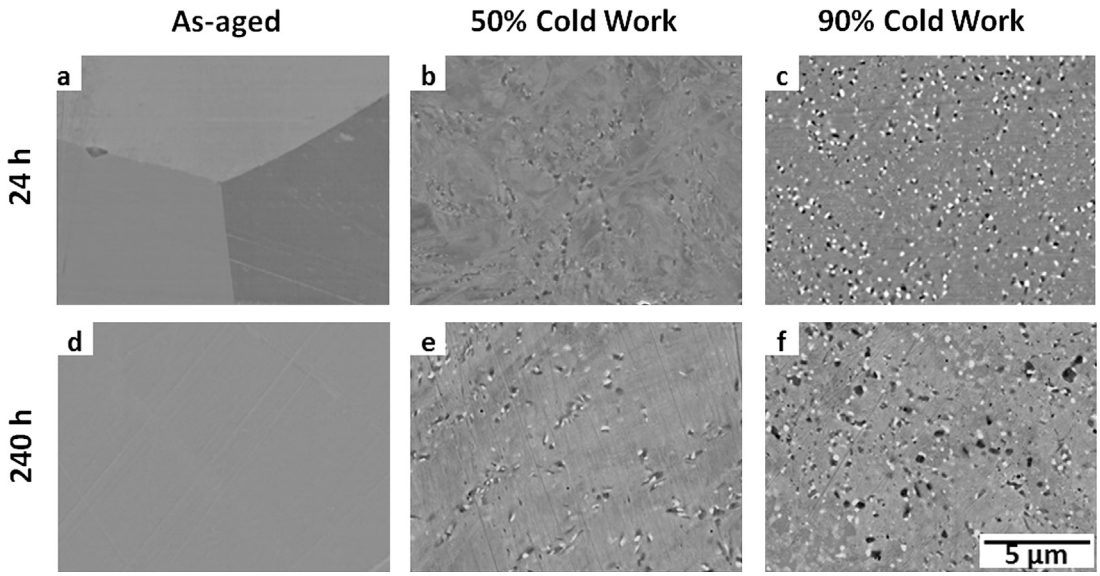

Fig. 4. Backscattered electron images from specimens aged at 700 °C: a) 24 h; b) 24 h after 50% cold work; c) 24 h after 90% cold work; d) 240 h; e) 240 h after 50% cold work; and f) 240 h after 90% cold work.

Fig. 5 shows the microstructural evolution of the alloy at 800 °C as a function of rolling reduction and annealing time. At 800 °C the microstructural response to aging and cold work was markedly different to that at 700 °C. NiAl and Laves phases precipitated at 800 °C, but Ni_3Al particles were not stable at this temperature. Unlike at 700 °C, at 800 °C with no cold work, precipitates are visible both in the matrix and on the grain boundaries after 2.4 h (Fig. 5(a)). The Laves phase precipitates are elongated. Precipitates on the grain boundary are larger than those in the matrix and there are no NiAl precipitates visible in the matrix, but they are present on the grain boundary. After 24 h there is a significant increase in the size of the Laves phase precipitates in the matrix and some are coupled with the B2-ordered NiAl precipitates (Fig. 5(d)). The Laves phase precipitates are needle-like and have several preferred orientations in the matrix. After 240 h more NiAl particles are present. From Fig. 5(g) they do not appear to be homogeneously distributed

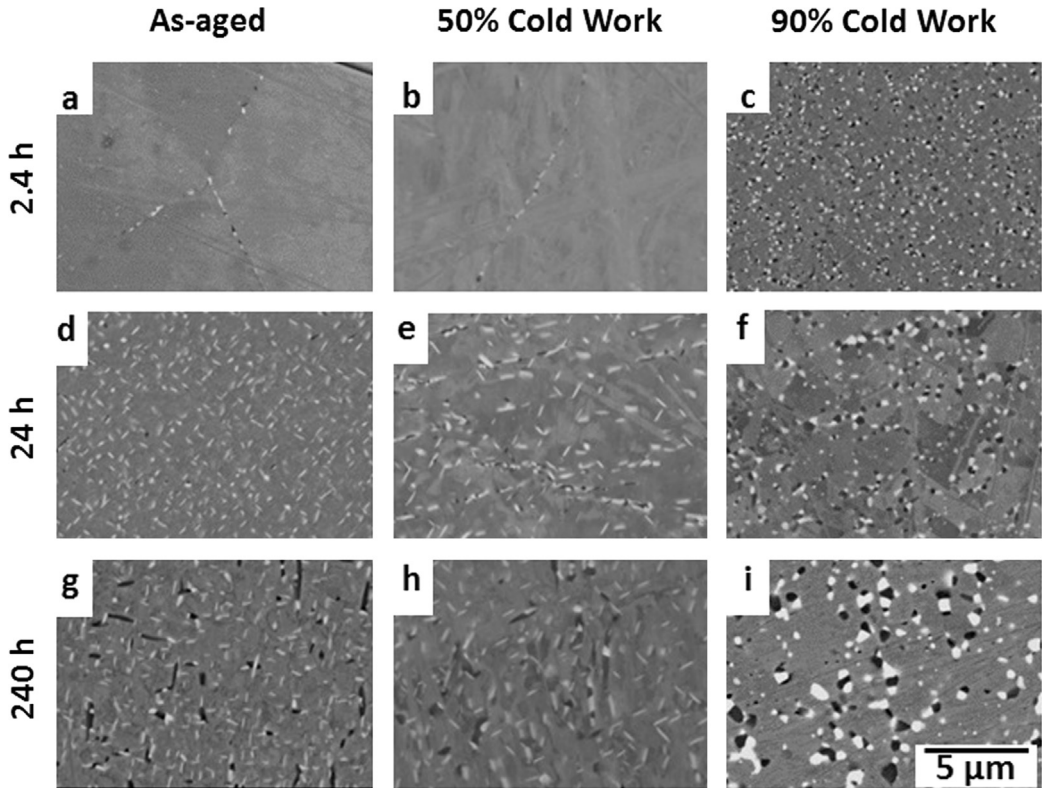

Fig. 5. Backscattered electron images from specimens aged at 800 °C: a) 2.4 h; b) 2.4 h after 50% cold work; c) 24 h after 90% cold work; d) 24 h; e) 24 h after 50% cold work, 24 h; f) 240 h after 90% cold work; g) 240 h; h) 240 h after 50% cold work; and i) 240 h after 90% cold work.

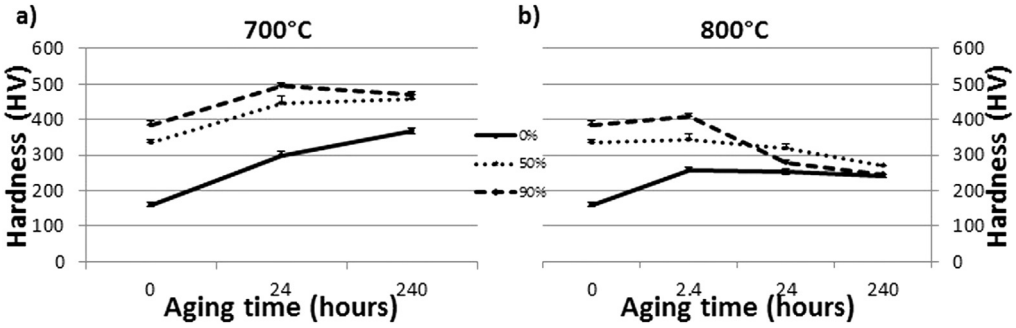

Fig. 6. Hardness values for samples annealed at a) 700 °C and b) 800 °C with error bars showing standard deviation of measurements.

in the matrix, but are co-located with Laves phase precipitates similar to the observations at 700 °C.

Faster precipitation kinetics after cold work were also observed at 800 °C as compared to 700 °C when holding the aging time constant at 2.4 h (Fig. 5(a)–(c))), 24 h (Fig. 5(d)–(f)), and 240 h (Fig. 5(f)–(i)). After 50% cold work Laves phase precipitates are present in the matrix and on the grain boundary (Fig. 5(b), (e) and (h)), displaying a preferred orientation relationship with the matrix as observed in the as-aged case. With 90% cold work (Fig. 5(f) and (i)) the microstructure more closely resembles that of the alloy with cold work at 700 °C. The Laves phase no longer appears elongated, but is granular in shape without any obvious preferred growth direction. Also, in the samples aged at 800 °C after 90% cold work on increasing the annealing time from 24 h to 240 h (Fig. 5(f) and (i)) it appears there is growth of both the Laves phase and B2 decorated subgrain boundaries. While Laves phase precipitation was the main target of this study, samples with 90% cold work highlight once again how cold work influenced the precipitation process so that Laves was concurrent with NiAl precipitation. For example, whereas it was noted that an aging treatment of 2.4 h at 800 °C (Fig. 5(a)) did not show significant NiAl precipitation, the same heat treatment after a 90% rolling reduction showed the matrix inundated with both NiAl and Fe_2Nb precipitates (Fig. 5(c)). Without cold work, the B2 NiAl precipitates were rarely observed in the matrix except for after long aging times (Fig. 5(g)).

In Fig. 6(a) the Vickers hardness of the solutionized alloy at 700 °C (~160 HV) increased with subsequent aging for 24 h and 240 h (~300 and ~367 HV respectively). 50 and 90% reductions prior to aging improved the hardness at each aging time by at least 90 HV compared to the as-aged state. Within the 240 h aging period, the alloy only shows a hardness peak (~495 HV) after a 90% rolling reduction prior to aging for 24 h. Subsequent aging to 240 h saw a slight decrease to ~471 HV. In a similar manner to the 700 °C aged samples, aging at 800 °C led to increased hardness after 50% and 90% rolling reductions prior to aging compared to the as-aged material at each time interval (Fig. 6(b)). However, for each reduction condition, there was an initial increase in hardness after 2.4 h and a subsequent decrease in hardness with further aging at 800 °C. For example, samples without cold work and those with reductions of 0%, 50%, and 90% saw hardness drop between aging at 2.4 h and 24 h.

4. Discussion

The above results show that cold rolling after solutionizing, but prior to aging, produces both more rapid precipitation of the Laves phase in the matrix and causes matrix precipitation of NiAl at 700 °C and 800 °C and of Ni_3Al at 700 °C. With aging, the Laves precipitates show a trend of initially fast growth followed by subsequent slower coarsening as observed in a 9CrW steel [28]. As

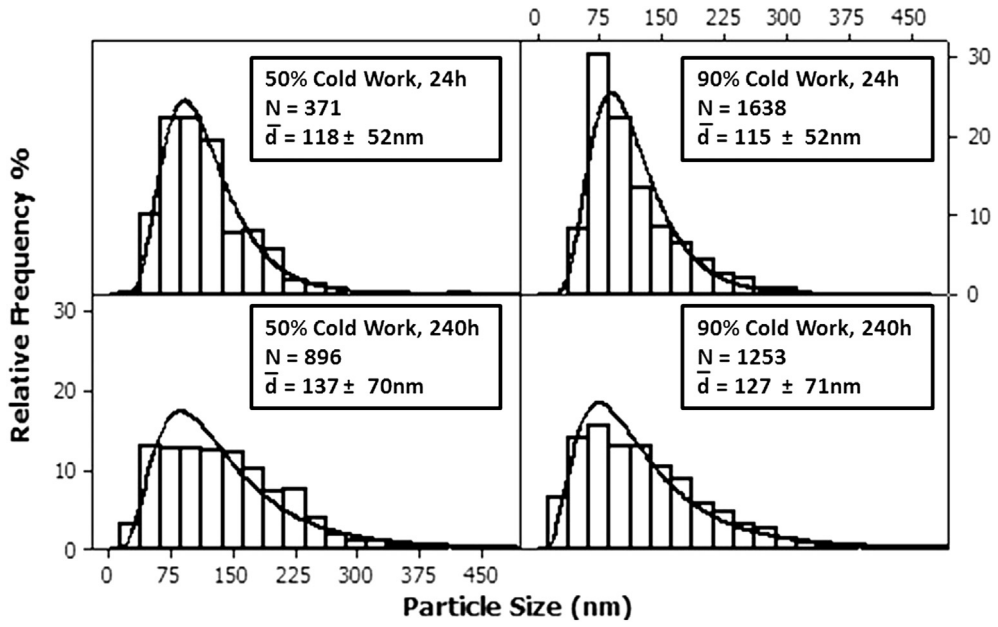

Fig. 7. Histogram plots of Laves phase particle size distributions for Fe–20Cr–30Ni–2Nb–5Al aged at 700 °C.

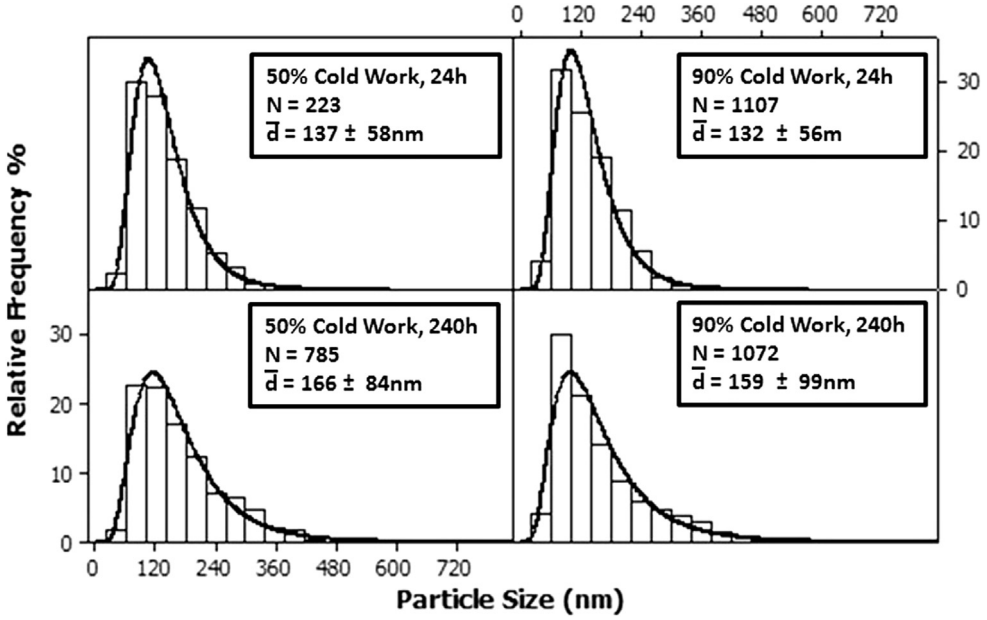

Fig. 8. Histogram plots of NiAl particle size distributions for Fe–20Cr–30Ni–2Nb–5Al aged at 700 °C.

observed in the work of Yamamoto et al. after creep-rupture of this alloy at 750 °C [17], when this alloy is simply aged at 800 °C the Laves phase is also plate-like in shape. Samples that were simply aged without prior cold work show precipitation trends similar to those observed by Takeyama [15] of the precipitation of Laves phase on the grain boundary and within the grain for the alloy Fe–20Cr–30Ni–2Nb after aging. The generated Time–Temperature-Precipitation (TTP) diagram showed that after aging for 1200 h at 800 °C Laves phase particles also precipitated homogeneously in the matrix with grain boundary precipitates being larger than those in the matrix. After 24 h at 800 °C the coarsening of the C14-type phase was mostly complete, except for where the C-14-type phase was coupled with the NiAl-type B2 phase. The Fe_2Nb and the NiAl phase has also shown thermal stability after 2160 h at 800 °C in an Fe–20Cr–15Ni–5Al-base alloy [14] and at 2012 h in other AFA alloys [16]. The Laves phase precipitates consistently grew along only a few directions within a given grain.

Image analysis of particle size at 700 °C (Figs. 7 and 8) and 800 °C (Figs. 9 and 10) provides insight into how aging and cold work impacted NiAl and Fe_2Nb precipitate growth. A lognormal distribution shows the best fit for most of the sample data. At 700 °C cold work induced precipitate formation of the Laves (Fig. 7) and B2–NiAl (Fig. 8). These precipitates saw modest increases in size when aging from 24 to 240 h. This early precipitate

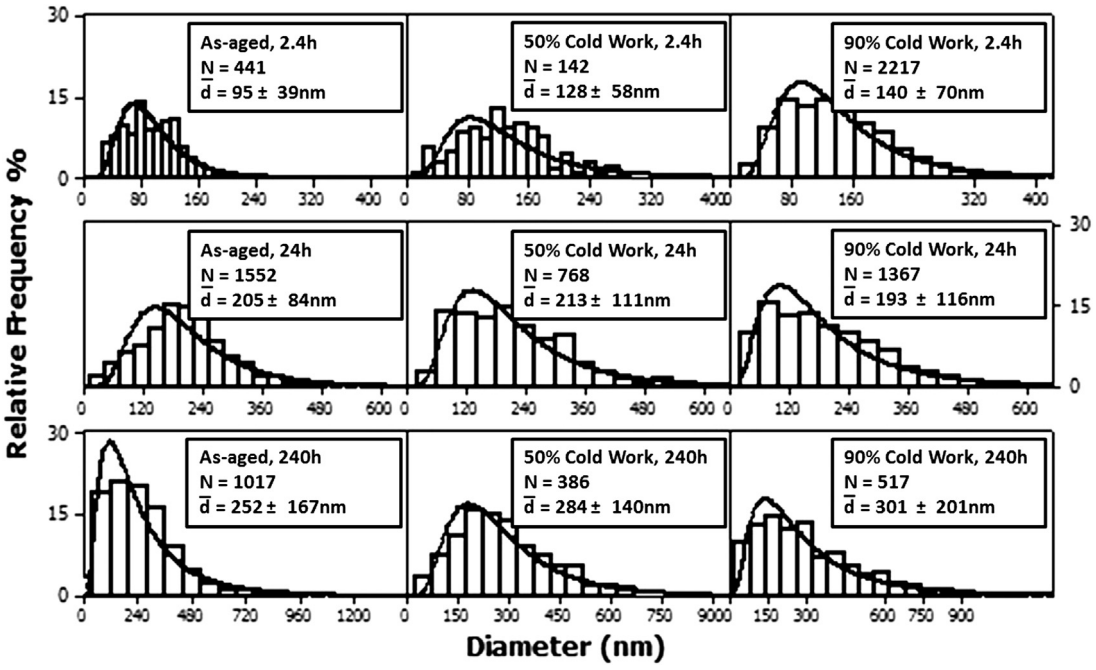

Fig. 9. Histogram plots of Laves particle size distributions for Fe–20Cr–30Ni–2Nb–5Al aged at 800 °C.

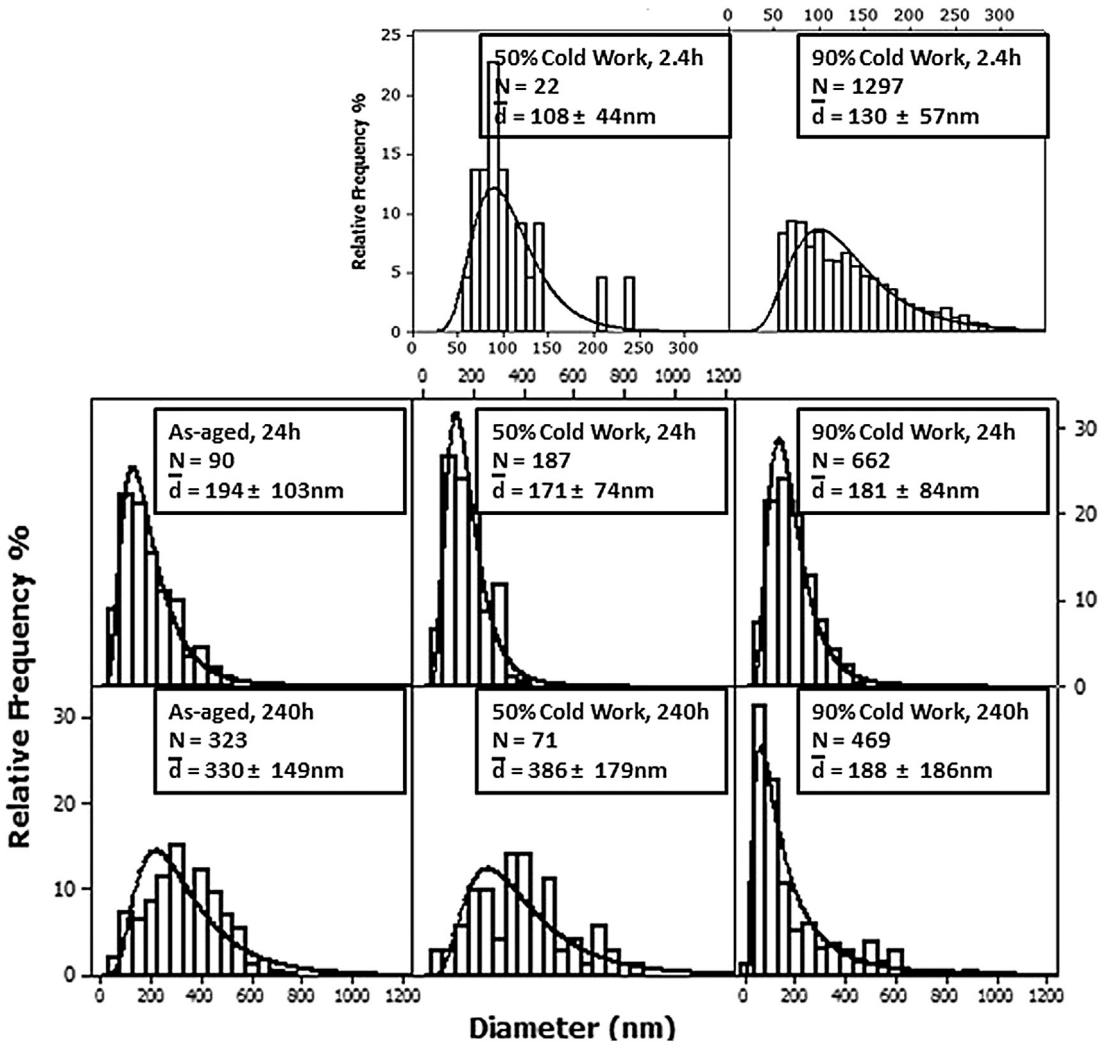

Fig. 10. Histogram plots of NiAl particle size distributions for Fe–20Cr–30Ni–2Nb–5Al aged at 800 °C.

formation would not have occurred with aging alone except at higher temperatures. This is an effect that has been seen in alpha-iron, where cold work samples caused precipitation to occur at a much lower temperature (250 °C) than in samples that had simply been aged (525 °C) and was also attributed to lattice defects increasing the diffusion of the precipitate-forming element [29]. At 800 °C with 0, 50% and 90% cold work both Laves and B2–NiAl precipitate sizes more than doubled when aging from 2.4 to 240 h (Figs. 9 and 10). The same was true for the NiAl except for the case of 90% cold work where the average particle size was relatively stable in going from 24 to 240 h. 50% cold work did not increase the volume fraction of precipitates compared to the as-annealed state, while 90% cold work led to a larger volume fraction of precipitates. In all cases, the standard deviation of the particle sizes increased with aging. TEM images of samples aged at the shorter 2.4 h interval showed very few particles existed below the data collection range used in the SEM so volume fraction results are expected not to be significantly impacted by SEM resolution limits.

A refined matrix that had reduced precipitate size and increased volume fraction was the desired microstructure for improved creep strength. In all cases up to 240 h at 700 °C Laves and NiAl particles did not show large increases in size and were ~30–70 nm above the upper 100 nm size limit (Figs. 7 and 8). At 800 °C while Laves particles initially started out in the 100 nm range, they grew to over 250 nm after aging at 240 h (Fig. 9). NiAl particle size increased to over 300 nm with just aging and with 50% cold work. Particle size did not increase as rapidly in going from 24 h (181 nm) to 240 h (188 nm) after 90% cold work (Fig. 10). Even though particles over 100 nm were observed after 240 h, cold working the material did lead to a higher volume fraction of precipitates. Despite particle growth at 700 °C and 800 °C, for each aging condition samples with 90% cold work had the highest total volume fraction of Laves and NiAl precipitates (Table 1).

The faster precipitation kinetics observed in the austenitic alloy Fe–20Cr–30Ni–2Nb–5Al after cold work is not unusual. For example, in as-cast FeNiMnAl alloys, β-Mn-structured particles only precipitate out after long anneals, but the high dislocation densities and large concentrations of vacancies in samples that have been mechanically milled accelerates their nucleation significantly [30]. Similarly, in 316 austenitic stainless steels, it was speculated that an acceleration of intermetallic precipitation could occur due to the speeding up of substitutional diffusion via an increased defect concentration. Laves-phase precipitation was accelerated after cold work and it was hypothesized that it was the result of increased diffusivity of elements that made up the Laves phase [20]. Takeyama's analysis indicated that in Fe–20Cr–30Ni–2Nb the formation of the Laves phase was controlled by Nb

Table 1
Volume fraction and standard deviations for NiAl and Laves phase particles.

Laves 700 °C			NiAl 700 °C		
Aging time (h)	50%	90%	Aging time (h)	50%	90%
24	1.0 ± 0.9	1.5 ± 0.4	24	0.5 ± 0.8	2.4 ± 1.4
240	3.1 ± 0.7	3.8 ± 0.8	240	3.9 ± 1.6	5.4 ± 1.2

Laves 800 °C				NiAl 800 °C			
Aging time (h)	0%	50%	90%	Aging time (h)	0%	50%	90%
2.4	0.7 ± 0.3	1.1 ± 1.0	3.9 ± 3.2	2.4	0.1 ± 0.1	0.3 ± 0.2	1.9 ± 2.5
24	7.1 ± 2.6	5.2 ± 1.5	6.0 ± 1.3	24	0.3 ± 0.1	0.9 ± 0.7	2.3 ± 0.9
240	6.5 ± 0.6	5.6 ± 1.2	9.8 ± 0.8	240	2.6 ± 0.7	1.7 ± 0.8	4.7 ± 0.9

diffusion in the austenite [15] and it follows in this case that the introduction of cold work into the alloy increased the diffusivity of the Laves phase forming elements in the austenitic matrix. In general, the distribution of the particles after cold work was non-uniform. At both 700 and 800 °C the alloy microstructure after cold work is not as homogeneous as for alloys that had simply been aged due to the presence of features such as deformation bands, cellular networks etc. The precipitation structure would most likely have been more uniform after deformation had particles been present during the rolling reduction, but since the starting point was a fully-solutionized matrix, their distribution was affected by the dislocation structures that were introduced by cold work [31].

Both the Laves and NiAl phases are no longer elongated and are instead globular after 90% cold work followed by aging at 800 °C. The globular precipitates observed after 50% cold work at 700 °C and 90% cold work at 800 °C appeared to have no preferred crystallographic orientation. A number of factors could have influenced this change in morphology. Their shape may have been influenced by their general appearance on grain boundaries and densely packed dislocations. Their concurrent precipitation also may have affected growth. When Takeyama compared Fe–20Cr–35Ni–2Nb to Fe–20Cr–25Ni–2Nb the Laves phase morphology was shown to change with the *c*/*a* ratio. It was also demonstrated that the alloy with decreased nickel content contained a Laves phase that was smaller and less elongated [15].

The hardness for the alloy aged at 700 °C is reflective of changes brought about by aging and cold work (Fig. 6(a)). As Laves and NiAl particles form their constituent atoms contribute less to solution strengthening and more to precipitate strengthening. At 700 °C after 50% cold work, hardness increases in conjunction with an increase in the volume fraction of both NiAl and Fe_2Nb precipitates. With 90% cold work there is increased hardness as compared to 50% cold worked samples with a peak in hardness at 24 h, the decrease at 240 h is most likely influenced by particle growth. The presence of the Ni_3Al particles most likely contributes to the higher hardness values seen at 700 °C compared with those seen at 800 °C. At 800 °C a hardness peak is not only observed after a 90% reduction, but also with a 50% reduction and by simply aging. The higher temperature is most likely the reason behind the increased aging rate due to the aforementioned enhanced diffusion through the matrix. At 800 °C with no cold work the single hardness peak is consistent with simple nucleation and precipitate growth. With the rise in the volume fraction of NiAl (0.3%–2.6%) the NiAl precipitates increase by nearly a third in size (194 vs. 322 nm), which may be the cause of the decrease in hardness (Fig. 6(b)). With 90% cold work, after aging at 800 °C for 24 h a large hardness decrease is congruent with the growth of recrystallized grains (Fig. 5(c)). After 240 h (244 Hv), the recrystallization that has occurred at 800 °C results in a hardness similar to the 240 h as-aged condition (242 HV).

5. Conclusions

Cold work resulted in the creation of a defect structure that facilitated the heterogeneous precipitation of both C14-type Fe_2Nb-type and B2-type NiAl precipitates. Increasing the amount of cold work caused the B2 phase to precipitate out after shorter anneals and at a lower temperature. Both B2 and Laves phases experienced more rapid precipitation in the matrix compared to material that had not been strained prior to aging at 700 °C and 800 °C. γ′-Ni_3Al precipitates were also noted after a 90% rolling reduction prior to aging at 700 °C. Rolling reductions of 50 and 90% followed by aging at 700 °C and a 90% rolling reduction followed by aging at 800 °C was shown to be effective in accelerating precipitation and refining the precipitates in Fe–20Cr–30Ni–2Nb–5Al. At 700 °C, cold work was effective in increasing precipitate volume fraction at each aging condition when compared to samples that were simply aged. The change in the kinetics occurring at the higher temperature of 800 °C influenced the effects of aging and cold work. For example, hardness peaks were observed with and without cold work. Precipitate size also generally increased. In the case of 90% cold work, the number density of precipitates only decreases with time even though the combined precipitate number density peaked and more than tripled within a short time period as compared to simply aged samples. Even when taking coarsening into consideration, with 90% cold work, the combined NiAl and Laves phase volume fraction increased. The increased precipitation caused by sufficient levels of cold work resulted in increased hardness when compared to material that had been simply aged.

Acknowledgments

Acknowledgment is made to the donors of the American Chemical Society Petroleum Research Fund #49157-ND10 and the National Science Foundation Grant DMR 1206240 for support of this research. The authors thank Dr. E.P. George of the Oak Ridge National Laboratory, Oak Ridge, TN for providing the ingots.

References

[1] Yamamoto Y, Brady MP, Lu ZP, Maziasz PJ, Liu CT, Pint BA, et al. Creep-Resistant, Al_2O_3-forming austenitic stainless steels. Science 2007;316:433–6.
[2] Brady MP, Yamamoto Y, Santella ML, Pint BA. Effects of minor alloy additions and oxidation temperature on protective alumina scale formation in creep-resistant austenitic stainless steels. Scr Mater 2007;57:1117–20.
[3] Brady M, Yamamoto Y, Santella M, Maziasz P, Pint B, Liu C, et al. The development of alumina-forming austenitic stainless steels for high-temperature structural use. JOM J Miner Metals Mater Soc 2008;60:12–8.
[4] Pint BA, Brady MP, Yamamoto Y, Santella ML, Howe JY, Trejo R, et al. Development of alumina-forming austenitic alloys for advanced recuperators. Proc ASME Turbo Expo 2009 Power Land Sea Air (GT2009) 2009;5:271–80.
[5] Pint BA, Shingledecker JP, Brady MP, Maziasz PJ. Alumina-forming austenitic alloys for advanced recuperators. Proc ASME Turbo Expo 2009: Power Land Sea Air (GT2007) 2007;3:995–1002.

[6] Brady MP, Yamamoto Y, Santella ML, Walker LR. Composition, microstructure, and water vapor effects on internal/external oxidation of alumina-forming austenitic stainless steels. Oxid Metals 2009;72:311–33.
[7] Yamamoto Y, Santella ML, Brady MP, Bei H, Maziasz PJ. Effect of alloying additions on phase equilibria and creep resistance of alumina-forming austenitic stainless steels. Metall Mater Trans A 2009;40:1868–80.
[8] Brady MP, Magee J, Yamamoto Y, Helmick D, Wang L. Co-optimization of wrought alumina-forming austenitic stainless steel composition ranges for high-temperature creep and oxidation/corrosion resistance. Mater Sci Eng A 2014;590:101–15.
[9] Yamamoto Y, Muralidharan G, Brady MP. Development of L12-ordered Ni_3(Al,Ti)-strengthened alumina-forming austenitic stainless steel alloys. Scr Mater 2013;69:816–9.
[10] Viswanathan R, Armor AF, Booras G. A critical look at supercritical power plants. Power 2004;148:42–9.
[11] Viswanathan R, Coleman K, Rao U. Materials for ultra-supercritical coal-fired power plant boilers. Int J Press Vessels Pip 2006;83:778–83.
[12] Viswanathan V, Purgert R, Rawls P. Coal-fired power materials. Adv Mater Process 2008;8:47–9.
[13] Viswanathan R, Henry J, Tanzosh J, Stanko G, Shingledecker J, Vitalis B, et al. US program on materials technology for ultra-supercritical coal power plants. J Mater Eng Perform 2005;14:281–92.
[14] Yamamoto Y, Brady MP, Lu ZP, Liu CT, Takeyama M, Maziasz PJ, et al. Alumina-forming austenitic stainless steels strengthened by Laves phase and MC carbide precipitates. Metall Mater Trans A 2007;38:2737–46.
[15] Takeyama M. Novel concept of austenitic heat resistant steels strengthened by intermetallics. Mater Sci Forum 2007;539–543:3012–7.
[16] Bei H, Yamamoto Y, Brady MP, Santella ML. Aging effects on the mechanical properties of alumina-forming austenitic stainless steels. Mater Sci Eng A 2010;527:2079–86.
[17] Yamamoto Y, Takeyama M, Lu ZP, Liu CT, Evans ND, Maziasz PJ, et al. Alloying effects on creep and oxidation resistance of austenitic stainless steel alloys employing intermetallic precipitates. Intermetallics 2008;16:453–62.
[18] Cahn JW. Nucleation on dislocations. Acta Metall 1957;5:169–72.
[19] Porter DA, Easterling KE. Phase transformations in metals and alloys. CRC; 1992.
[20] Weiss B, Stickler R. Phase instabilities during high temperature exposure of 316 austenitic stainless steel. Metall Mater Trans B 1972;3:851–66.
[21] Zhang C, Enomoto M, Yamashita T, Sano N. Cu precipitation in a prestrained Fe-1.5 wt pct Cu alloy during isothermal aging. Metall Mater Trans A 2004;35:1263–72.
[22] Sitarama Raju K, Subramanya Sarma V, Kauffmann A, Hegedűs Z, Gubicza J, Peterlechner M, et al. High strength and ductile ultrafine-grained Cu–Ag alloy through bimodal grain size, dislocation density and solute distribution. Acta Mater 2013;61:228–38.
[23] Niranjani VL, Hari Kumar KC, Subramanya Sarma V. Development of high strength Al–Mg–Si AA6061 alloy through cold rolling and ageing. Mater Sci Eng A 2009;515:169–74.
[24] Ringer SP, Muddle BC, Polmear IJ. Effects of cold work on precipitation in Al–Cu–Mg–(Ag) and Al–Cu–Li–(Mg–Ag) alloys. Metall Mater Trans A 1995;26:1659–71.
[25] Maziasz P. Developing an austenitic stainless steel for improved performance in advanced fossil power facilities. JOM J Miner Metals Mater Soc 1989;41:14–20.
[26] Ashby MF, Jones DRH. Engineering materials 2: an introduction to microstructures and processing. Pergamon Press; 1986.
[27] Schneider CA, Rasband WS, Eliceiri KW. NIH image to imagej: 25 years of image analysis. Nat Meth 2012;9:671–5.
[28] Korcakova L, Hald J, Somers MAJ. Quantification of laves phase particle size in 9CrW steel. Mater Charact 2001;47:111–7.
[29] Soeno K. Effect of cold work on the precipitation of copper from alpha-iron. Trans JIM 1970;11.
[30] Wu X, Baker I, Wu H, Munroe PR. Accelerated precipitation due to mechanical milling of two-phase $B2/L2_1Fe_{30}Ni_{20}$ $Mn_{20}Al_{30}$. J Alloys Compd 2013;559:97–100.
[31] Humphreys FJ, Hatherly M. Recrystallization and related annealing phenomena. Elsevier; 1995.